Commun Nonlinear Sci Numer Simulat 84 (2020) 105208

Contents lists available at ScienceDirect

Commun Nonlinear Sci Numer Simulat

journal homepage: www.elsevier.com/locate/cnsns

Research paper

Long-range memory effects in a magnetized Hindmarsh-Rose neural network

Armand S. Etémé[a,*], Conrad B. Tabi[a,b], Alidou Mohamadou[c], Timoléon C. Kofané[a,b]

[a] Department of Physics, Faculty of Science, University of Yaoundé I, P.O. Box 812, Yaoundé, Cameroon
[b] Botswana International University of Science and Technology, P/Bag 16 Palapye, Botswana
[c] Department of Physics, Faculty of Science, University of Maroua, P.O. Box 46, Maroua, Cameroon

ARTICLE INFO

Article history:
Received 16 April 2019
Revised 23 December 2019
Accepted 27 January 2020
Available online 28 January 2020

Keywords:
Modulational instability
Chaos
Synchronization
Chimera states

ABSTRACT

We consider a model network of diffusively coupled Hindmarsh-Rose neurons to study both analytically and numerically, long-range memory effects on the modulational instability phenomenon, chaotic, synchronous and chimera states within the network. The multiple scale method is used to reduce the generic model into a discrete nonlinear Schrödinger equation. The latter is explored in the linear stability analysis and the instability criterion along with the critical amplitude are derived. The analytical results predict that strong local coupling, high electromagnetic induction and strong long-range interactions may support the formation of highly localized excitations in neural networks. Through numerical simulations, the largest Lyapunov exponents are computed for studying chaos, the synchronization factor and the strong of incoherence are recorded for studying, respectively synchronous and chimera states in the network. We find the appropriate domains of space parameters where these rich activities could be observed. As a result, quasi-periodic synchronous patterns, chaotic chimera and synchronous states, strange chaotic and non-chaotic attractors are found to be the main features of membrane potential coupled with memristive current during long-range memory activities of neural networks. Our results suggest that a combination of long-range activity and memory effects in neural networks may produces a rich variety of membrane potential patterns which are involved in information processing, odors recognition and discrimination and various diseases in the brain.

1. Introduction

The memory effects inherent to the neural networks have the capability, even in the absence of stimulus-like external current, to generate and sustain neuronal electrical activity when the electromagnetic induction magnitude reaches a certain threshold [1,2]. Indeed, Wu et al. [1] have studied electrical activity in a Fitzhugh-Nagumo (FHN) cardiac model [3] under electromagnetic induction. They reported that the collective behaviors of myocardial cells and electrical modes are much dependent on the distribution of magnetic flux. Moreover it is indicated that electromagnetic induction can change the

* Corresponding author.
E-mail addresses: etemearmand@yahoo.fr (A.S. Etémé), conrad@aims.ac.za, tabic@biust.ac.bw (C.B. Tabi), mohdoufr@yahoo.fr (A. Mohamadou), tckofane@yahoo.com (T.C. Kofané).

https://doi.org/10.1016/j.cnsns.2020.105208
1007-5704/

formation of spatial patterns and electrical activities of myocardial cells. Along the same line, Etémé et al. [2] have investigated firing and synchronization modes in a Hindmarsh-Rose (HR) neuronal model [4] under magnetic stimulation. They found that neuronal electrical activity induced by electromagnetic induction of intra-and extracellular media is governed by two main neurodynamics regimes namely, the spiking regime at the low induction and the bursting regime at the high induction. Additionally, the memory effects induced by the fluctuation of internal magnetic flux could lead neural network from an incoherent to a coherent states at weak local coupling ($D = 0.01$), D being the diffusive coupling strength between nearest-neighbor neurons. In certain circumstances, local coupling seems to be inappropriate in the transmission of neural information in a given neuronal population thus restricting some brain functions such as visual perception [5]. Consequently, the long-range interactions (LRIs) become essential.

During the last decades, effects of LRI on the regulation of some biological processes have been increasingly studied in different biological systems such as DNA [6,7], α-helix proteins [8,9] and neural networks [5,10–12]. In visual perception, the perception of illusory contours, area contrast, color constancy, depth plane, coherent motion and texture contrast requires neurophysiological mechanisms within the visual pathways with LRI [5]. Indeed, the release of neurotransmitters at synaptic junctions would promote long-range (LR) communication between different neurons via nonlinear couplings. This also suggests that the LRIs could ensure neuronal communication even in the event of defection of one or several neurons in a given neural network. In our previous contributions [12,13], effects of LR communication have been considered in investigating patterns formation and cooperative behaviors by handling a well-known one-dimensional HR model. It was found that LR connections among neurons strongly affect cerebral activities which are mainly characterized by coherent (in the case of weak LRI) and incoherent (in the case of strong LRI) nonlinear spatiotemporal patterns at weak local coupling. Although the strong LRI regime became synchronous by increasing the diffusive coupling strength up to a suitable value [12]. As well, Mvogo *and* its coworkers [11] have studied the properties of localized waves in the diffusive HR neural networks with LRI modelled by fractional-order differential equations. They shown that LR diffusive couplings could be perceived as a way to transport information via nonlinear waves both in spatial and temporal dimensions for specific processes of the brain to be controlled.

Soliton-like unperturbed localized waves have the great importance in the conduction of action potential along a nerve fiber, since they can preserve density, velocity or amplitude of neuronal information. Such localized waves are well-known to be generated by modulational instability (MI) phenomenon [12–18] under the competitive effects of nonlinearity and dispersion in a given lattice. Additionally, MI and synchronization phenomena are believed to run in the same manner in a given dynamical system. Accordingly, Etémé et al. [12] have demonstrated that more the connected neural chains are modulationally unstable, more they become synchronically stable. The previous findings have been dealt with while taking into consideration the external current as a neuro-stimulator. In the present framework we include in the so-called magnetized neural model [2], effects of LRI to study the possibility of modulated synchronous patterns to rise within the system. To do so, the competitive effects of electromagnetic induction, LRI degree and local coupling force are evaluated on the substantiality of such patterns.

The rest of the paper deals in Section 2 with the presentation of mathematical model and the multi-scaling approach allowing to reduce the generic model into a discrete nonlinear Schrödinger (DNLS) equation with coefficients-dependence on the control parameters. In Section 3, MI is analytically examined and the instability criterion along with the critical amplitude expression are derived. Some features of MI including, critical amplitude, envelope soliton amplitude are displayed followed by valuable comments on space parameters which could sustain a such behavior. The important role of complex group velocity in neuronal systems as an active and absorbing media has been also highlighted. Section 4 presents the numerical experiment on chaos, synchronous and chimera sates in neural network. We summarize our work in Section 5 by concluding remarks and future explorations.

2. Model and discrete multiscale analysis

Very recently, we have developed a new mathematical HR model where neural electrical activity is exclusively stimulated by means of electromagnetic induction [2], whereas, several models where such activity is provoked either by external current [12–14,19,20] or by DNA signaling [21] have been previously investigated. Here we consider a model of [2] by including the LR diffusive effects in order to investigate the partnership between intrinsical memristive and boundary long-range couplings on modulated waves along a chain made of N identical neurons. As a result, the mathematical model is given by

$$\begin{aligned}
\dot{x}_n &= y_n - ax_n^3 + bx_n^2 - z_n - k_1 w(\phi_n)x_n + \sum_{j=1}^{J} D_j(s)(x_{n+j} - 2x_n + x_{n-j}),\\
\dot{y}_n &= c - dx_n^2 - ey_n,\\
\dot{z}_n &= \Omega_0^2(x_n - x_e) - rz_n,\\
\dot{\phi}_n &= x_n - k_2\phi_n + \phi_0,
\end{aligned} \tag{1}$$

where the state variables x_n, y_n, z_n and ϕ_n, respectively, represent the action membrane potential, the fast ionic current, the slow ionic current and the magnetic flux within neuron n, $\Omega_0^2 = r\kappa$.

The function $w(\phi_n)x_n$ stands for the memristive current [22–24] i_n, where $w(\phi_n)=\cos(\phi_n)$ [2] represents the memductance which translates the memory effect of the memristor. It is easy to approximate the function $w(\phi_n)$ to $w(\phi_n)=\alpha+3\beta\phi_n^2$ with $\alpha=1$ and $\beta=-1/6$ for the system of Eq. (1) to be handled analytically. The s-dependent coefficient $D_j(s)=D|j|^{-s}$ indicates the LR diffusive coupling strength with constant intensity D, j which suits up to J, is the normalized distance between two interacting neurons in the network, J being the range of interaction, which gives an idea on the spatial expansion of LR coupling. Parameters k_1 and ϕ_0, are the magnetic coupling strength on the one hand and external electromagnetic induction on the other hand. Here ϕ_0 will be considered as a time-independent parameter. The constant model parameters are fixed as: $a=1.0$, $b=3.0$, $c=1.0$, $d=5.0$, $e=1.0$, $r=0.006$, $\kappa=4.0$, $x_e=-1.60$, $k_2=0.5$ and $\phi_0=1.0$, while D, s and k_1 will be considered as the control parameters. The nonlinear Eq. (1) which includes the intrinsical memristive coupling term $k_1\cos(\phi_n)x_n$ and the boundary LR coupling term $\sum_{j=1}^{J}D|j|^{-s}(x_{n+j}-2x_n+x_{n-j})$ constitutes a new class of neural models where the interplay between nonlinearity and dispersion should give rise to a nonlinear localized soliton-like solutions known as the best tool in the transport and transfer of nerve impulses within neural networks [12–14,19,25–27]. In order to demonstrate the existence of such solutions, we propose to firstly reduce Eq. (1) into a DNLS equation by applying the technic of multiple scale expansion [10,13,18,26,28,29].

The approach based on discrete multiscale analysis, while considering boundary value problems, supposes that solution $s_n(t)=\{x_n(t),y_n(t),z_n(t),\phi_n(t)\}$ of Eq. (1) can be developed in a Taylor series in power of the small parameter ϵ measuring the amplitude of the initial wave. That is to say

$$s_n(t)=\sum_{p=1}^{\infty}\epsilon^p\sum_{l=-p}^{p}S_p^{(l)}(m,\tau)A^{(l)}(n,t), \tag{2}$$

where $S_p^{(l)}(m,\tau)=\{X_p^{(l)}(m,\tau),Y_p^{(l)}(m,\tau),Z_p^{(l)}(m,\tau),\Phi_p^{(l)}(m,\tau)\}$ obeys to the real valuedness condition $S_p^{(-l)}(m,\tau)=(S_p^{(l)}(m,\tau))^*$, * being the complex conjugate. $A^{(l)}(n,t)=e^{il(Qn+\Omega t)}$ represents the carrier wave that is modulated with the envelope solution $S_p^{(l)}(m,\tau)$ to form the general solution $s_n(t)$ at the perturbation of order p for a given harmonic $l\le p$. The angular frequency Ω and the wavenumber Q of the carrier wave are usually related by a single nonlinear dispersion relation. The slow scaling variables m and τ are defined as:

$$m=\epsilon^2 n,\ \tau=\epsilon(t+n/v_g), \tag{3}$$

where v_g designates the group velocity which will be found later under the Fredholm solvability condition. The main formula allowing to perform the diffusive term $(x_{n+j}-2x_n+x_{n-j})$ is given by

$$\begin{aligned}x_{n+j}-2x_n+x_{n-j}=&\Big[A^{(l)}(n+j,t)-2A^{(l)}(n,t)+A^{(l)}(n-j,t)\Big]X_p^{(l)}(m,\tau)\\&+\epsilon\Big[A^{(l)}(n+j,t)-A^{(l)}(n-j,t)\Big]\Big(\frac{j}{v_g}\Big)\frac{\partial}{\partial\tau}X_p^{(l)}(m,\tau)+\frac{\epsilon^2}{2}\Big[A^{(l)}(n+j,t)+A^{(l)}(n-j,t)\Big]\\&\times\Big(\frac{j}{v_g}\Big)^2\frac{\partial^2}{\partial\tau^2}X_p^{(l)}(m,\tau)+\frac{\epsilon^2}{2}\Big[A^{(l)}(n+j,t)-A^{(l)}(n-j,t)\Big]\Big[X_p^{(l)}(m+j,\tau)-X_p^{(l)}(m-j,\tau)\Big].\end{aligned} \tag{4}$$

Inserting solution (2) into Eq. (1), we get

$$\begin{aligned}&X_1^{(0)}=Y_1^{(0)}=Z_1^{(0)}=\Phi_1^{(0)}=0,\ X_1^{(1)}=\eta,\ Y_1^{(1)}=0,\ Z_1^{(1)}=\frac{\Omega_0^2}{r+i\Omega}\eta,\ \Phi_1^{(1)}=\frac{1}{k_2+i\Omega}\eta,\\&X_2^{(0)}=\frac{2(eb-d)}{e(\kappa+\alpha k_1)}|\eta|^2,\ Y_2^{(0)}=-\frac{2d}{e}|\eta|^2,\ Z_2^{(0)}=\frac{2\kappa(eb-d)}{e(\kappa+\alpha k_1)}|\eta|^2,\ \Phi_2^{(0)}=\frac{2(eb-d)}{k_2e(\kappa+\alpha k_1)}|\eta|^2,\\&X_2^{(1)}=\chi,\ Y_2^{(1)}=0,\ Z_2^{(1)}=\frac{1}{r+i\Omega}\Big(\Omega_0^2\chi-\frac{\Omega_0^2}{r+i\Omega}\frac{\partial\eta}{\partial\tau}\Big),\ \Phi_2^{(1)}=\frac{1}{k_2+i\Omega}\Big(\chi-\frac{1}{k_2+i\Omega}\frac{\partial\eta}{\partial\tau}\Big),\\&X_2^{(2)}=a_2^{(2)}\eta^2,Y_2^{(2)}=-\frac{d}{e+2i\Omega}\eta^2,\ Z_2^{(2)}=\frac{\Omega_0^2}{r+2i\Omega}a_2^{(2)}\eta^2,\ \Phi_2^{(2)}=\frac{1}{k_2+2i\Omega}a_2^{(2)}\eta^2,\ X_3^{(0)}=a_3^{(0)}\frac{\partial|\eta|^2}{\partial\tau},\\&Y_3^{(0)}=-\frac{2d}{e}\frac{\partial|\eta|^2}{\partial\tau},\ Z_3^{(0)}=\Big(\frac{a_3^{(0)}}{r}-\frac{2\kappa(eb-d)}{\kappa e+\alpha k_1}\Big)\frac{\partial|\eta|^2}{\partial\tau},\ \Phi_3^{(0)}=\Big(\frac{a_3^{(0)}}{k_2}-\frac{2(eb-d)}{k_2^2(\kappa e+\alpha k_1)}\Big)\frac{\partial|\eta|^2}{\partial\tau},\end{aligned} \tag{5}$$

where $\eta=\eta_m(\tau)$ and $\chi=\chi_m(\tau)$ are the unknown functions, and

$a_2^{(2)}=(r+2i\Omega)\big(b(e+2i\Omega)-d\big)\Delta_1^{-1}$, $a_3^{(0)}=\frac{2dr}{e+\alpha rk_1}+\frac{2(eb-d)(r+\kappa)}{(e+\alpha rk_1)(\kappa e+\alpha k_1)}$

$\Delta_1=\big(e+2i\Omega\big)\Big(\Omega_0^2+\big(r+2i\Omega\big)\Big(2i\Omega+\alpha k_1+4\sum_{j=1}^{J}D_j(s)\sin^2(jQ)\Big)\Big)$.

The dispersion relation found at the order (ϵ^1, l=1) is given by

$$(i\Omega)^2+\left(r+\alpha k_1+4\sum_{j=1}^{J}D_j(s)\sin^2\left(\frac{jQ}{2}\right)\right)(i\Omega)+\left(\Omega_0^2+\alpha rk_1+4r\sum_{j=1}^{J}D_j(s)\sin^2\left(\frac{jQ}{2}\right)\right)=0, \tag{6}$$

and the group velocity derived from the Fredholm solvability condition at order $(\epsilon^2, l=1)$ should be verified as

$$v_g = \frac{\partial \Omega}{\partial Q} = \frac{2i(r+i\Omega)^2 \sum_{j=1}^{J} D_j (1-s)\sin(jQ)}{(r+i\Omega)^2 - \Omega_0^2}. \tag{7}$$

By solving the dispersion relation given by Eq. (6), we found real solutions in $(i\Omega)$, that is to say, the angular frequency Ω is purely imaginary. Hence, the group velocity given in Eq. (7) can be rewritten in the form $v_g = ic_g$, where c_g designates the imaginary part of the complex group velocity v_g. From above, it is well-understood that both angular frequency of carrier wave and group velocity of envelop soliton are fully imaginary complex numbers. This is commonly met in absorbing and active media [30] where the imaginary parts of both angular frequency and group velocity are involved in temporal attenuation of the signal.

The order $(\epsilon^3, l=1)$, after made some simplifications yields the dynamics equation for $\eta_m(\tau)$ as

$$i\sum_{j=1}^{J} \rho_j(s)\left(\eta_{m+j} - \eta_{m-j}\right) + \sigma \frac{\partial^2 \eta_m}{\partial \tau^2} + \gamma |\eta_m|^2 \eta_m = 0, \tag{8}$$

with

$$\rho_j(s) = D_j(s)\sin(jQ),\ \sigma = -\frac{\Omega_0^2}{(r+i\Omega)^3} - \frac{\left[(r+i\Omega)^2 - \Omega_0^2\right]^2 \sum_{j=1}^{J} D_j(2-s)\cos(jQ)}{4(r+i\Omega)^4\left(\sum_{j=1}^{J} D_j(1-s)\sin(jQ)\right)^2},$$

$$\gamma = -3\left(a + \frac{3\beta k_1}{(k_2+i\Omega)^2}\right) + 2\left(b - \frac{d}{e+i\Omega}\right) \times \left(\frac{2(eb-d)}{e(\kappa+\alpha k_1)} + \frac{(r+2i\Omega)\left(b(e+2i\Omega)-d\right)}{\Delta_1}\right). \tag{9}$$

The differential-difference equation Eq. (8) where the diffusive coefficient $\rho_j(s)$, the dispersion coefficient σ and the nonlinearity coefficient γ are all real constitutes a DNLS equation. Similar equations have been early found in the broad range of physical systems for investigating MI phenomenon [10,13,26,29,31]. In this framework, a such phenomenon will be studied with a particular attention of long-range memory effects on synchronization and chaotic behavior of neural network.

3. Linear stability analysis

A plane wave as $\eta_m(\tau) = \eta_0 e^{i(\nu m - \mu\tau)}$ is considered to be a solution of amplitude Eq. (8), where the amplitude η_0, the wavenumber ν and the angular frequency μ verify the following discrete nonlinear dispersion relation

$$\mu^2 = \delta\left[|\eta_0|^2 - \frac{2}{\gamma}\sum_{j=1}^{J} \rho_j(s)\sin(j\nu)\right], \tag{10}$$

with $\delta = \gamma/\sigma$. Complex solutions in μ exist if the following instability criteria

$$\delta < 0, \tag{11}$$

$$|\eta_0|^2 > \frac{2}{\gamma}\sum_{j=1}^{J} \rho_j(s)\sin(j\nu) = \eta_{0,cr}^2, \tag{12}$$

are simultaneously fulfilled, so that $\mu = i\lambda$. Moreover, the boundary function $\sin(j\nu)$ should be equal to unity for $\eta_{0,cr}$ to reach its maximum value, that is to said $\nu j = \pi/2$. So, the positive real $\lambda = \sqrt{-\delta\left[|\eta_0|^2 - \frac{2}{\gamma}\sum_{j=1}^{J}\rho_j(s)\right]}$. Eq. (11) defines a large spectrum of wavenumbers Q in which modulated waves are spatially expected, whereas Eq. (12) defines the critical amplitude above which such patterns arise within the network. Some former studies [10,13] have proven that the condition of Eq. (11) is satisfied when $0 < Q \leq Q_{cr}$, Q_{cr} being the critical wavenumber of the carrier wave above which the plane wave remains stable. This result is still verified here by numerically solving Eq. (11). In this framework, we have adopted $Q = 0.01\pi$ to investigate modulated waves within the system under the variation of the coupling intensity D, the power s of LR interaction and the magnetic coupling strength k_1 while fixing $J = 10$ in order to limit LRI to the first twenty neighbors.

Furthermore, it is worth noticing that the instability described in the present work results from wave scattering in a nonlinear medium (boundary value problem) which requires one to use a change of variables like $m = \epsilon^2 n$ and $\tau = \epsilon(t + n/v_g)$, which in turn leads to the unstable wave DNLS equation for the envelope $\eta_m(\tau)$. The resulting instability is then of first order (a second perturbation analysis of the equation for the envelope is not required), and has for boundary value problems the same universal character as the Benjamin-Feir instability [32] has for initial value problems. Indeed, the Benjamin-Feir instability describes the mechanism of the exponential growth of the modulation of a wave evolving in a continuous nonlinear dispersive medium while in the discrete instability which is developed here, the plane wave becomes uniformly unstable if its amplitude η_0 exceeds a threshold value $\eta_{0,cr}$ for any wavenumber Q beyond the zero of the group velocity dispersion. The above report accurately corroborates with the investigations which were made by Leon and Manna [18] while studying discrete instability in nonlinear sine-Gordon and Toda lattices.

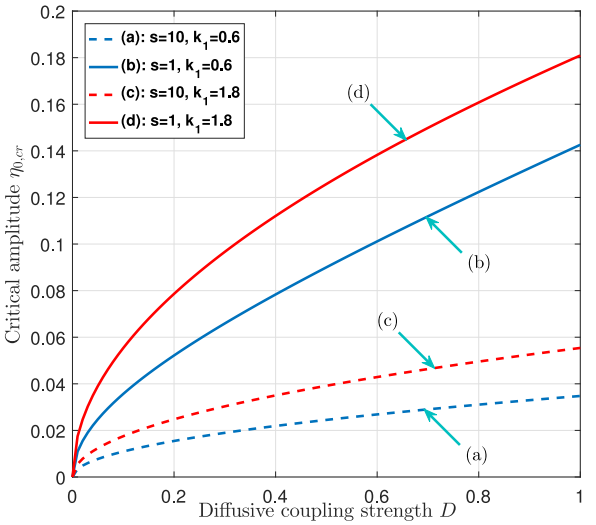

Fig. 1. (Color online) The panel shows the critical amplitude $\eta_{0,cr}$ versus the coupling intensity D under the change of parameters s and k_1 as written in the window. Curves (a) and (b) correspond to weak LRI ($s = 10$), while curves (c) and (d) are for strong LRI ($s = 1$). In both cases (weak and strong LRI), effects of spiking regime ($k_1 = 0.6$) and bursting regime ($k_1 = 1.8$) on critical amplitude are investigated. Increasing parameters D and k_1 increases the critical amplitude thus predicting that high values of D and k_1 could support MI phenomenon within a magnetized neural tissues. However, reversible effects are observed with increasing parameter s.

In practice the onset of modulational instability under the discrete instability mechanism occurs when the angular frequency μ of a plane wave solution $\eta_m(\tau)$ become complex, i.e., $\mu = i\lambda$. Therefore the solution of envelop shape is transformed into

$$\eta_n(t) = \eta_0 e^{\epsilon\lambda t} \times \exp[i\epsilon(\epsilon - \lambda/c_g)n]. \tag{13}$$

From above solution Eq. (13), it is clear that the plane wave amplitude is not yet constant, instead grows exponentially as time t increases. Hence, the envelope soliton amplitude $\eta_0(t) = \eta_0 e^{\epsilon\lambda t}$ constitutes the substantial issue of discrete instability. In the following, we will examine the dependence of both critical amplitude $\eta_{0,cr}$ and envelop soliton amplitude $\eta_0(t)$ on the space control parameters including also effects of time t and imaginary part c_g of the group velocity.

The features of (Fig. 1) shows the plot of critical amplitude $\eta_{0,cr}$ versus the diffusive coupling strength D for both spiking ($k_1 = 0.6$) and bursting ($k_1 = 1.8$) regimes, in weak ($s = 10$) and strong ($s = 1$) LRI. In recall, the weak LRI is supposed to reduce interactions into a nearest-neighbor situation, while the strong LRI means that each lattice n in the network interacts with all its first twenty neighbors. The spiking and bursting values of magnetic coupling strength k_1 have been chosen in accordance with [2]. Here the results report that critical amplitude $\eta_{0,cr}$ increases with coupling intensity D, the magnetic coupling strength k_1 and decreases with the power s of the LRI. The above issues predict that in the magnetized HR neural model, bursting electrical activity is more unstable than spiking one and could be considered as a more suitable mode in neural information processing within the brain. In other words, heavy electromagnetic induction better supports modulated waves in neural tissues than the lowly process. It is also indicated that the memory effects induced by the variation of the magnetic flux of intracellular medium may be accentuated by strong LRI, i.e., a small values of parameter s. In short, we can predict from above that the generic magnetized HR neural model given by Eq. (1) may support the propagation of soliton waves known as the best tool in conducting and transmitting of the nerve impulse within neural networks. The phenomenon is emphasized by high electromagnetic induction, strong local coupling and strong LRI.

Now we are going to examine the features of envelope soliton amplitude $\eta_0(t)$ given by Eq. (13). The results are presented on Figs. 2 and 3 when one especially considers weak instability ($s = 10$ and $k_1 = 0.6$) in panel (a) and strong instability ($s = 1$ and $k_1 = 1.8$) in panel (b). In Fig. 2 where $\eta_0(t)$ is plotted as a function of D, we realize that initial amplitude η_0 of the plane wave does not remain constant instead grows with the time, also with others control parameters. Another fact is that the magnitude of envelope soliton amplitude is greater in weak instability situation than in strong instability one. This observation was obviously foreseeable since the large values of the critical amplitude are associated with the small values of the modulation parameter λ. In Fig. 3, the envelope soliton amplitude is plotted versus time t under the change of imaginary part c_g of the group velocity v_g. We notice that as c_g increases, the magnitude of envelope soliton amplitude decreases in time. Furthermore, bursting regime appears to be very sensitive to the change of parameter c_g since the envelope soliton amplitude drastically decreases even for the low variation of parameter c_g. All these issues confirm that the complex group velocity is involved in temporal attenuation of envelope soliton signal within absorbing and active media such as neural networks. Moreover, the more powerful the dynamical regime, the more the phenomenon of attenuation.

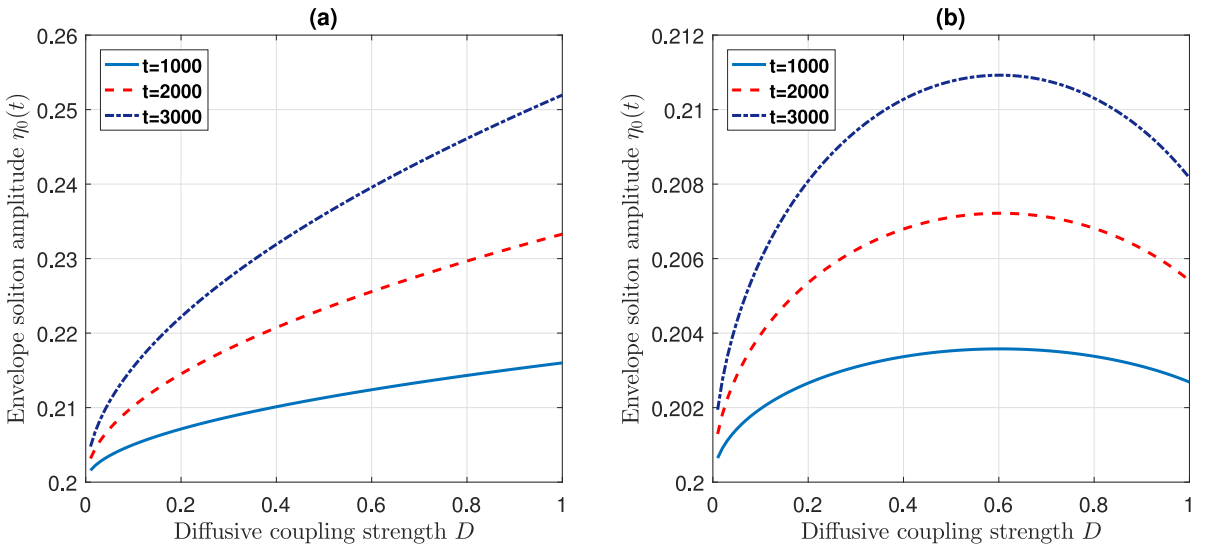

Fig. 2. (Color online) Variations of envelope soliton amplitude $\eta_0(t)$ versus the diffusive coupling strength D when propagation time t increases as displayed in each panels. In panel (a), weak LRI ($s = 10$) and spiking regime ($k_1 = 0.6$) is considered, while in panel (b), strong LRI ($s = 1$) and bursting regime ($k_1 = 1.8$) is examined. In both cases, we see how envelope soliton amplitude increases with the time and takes high values in the first case.

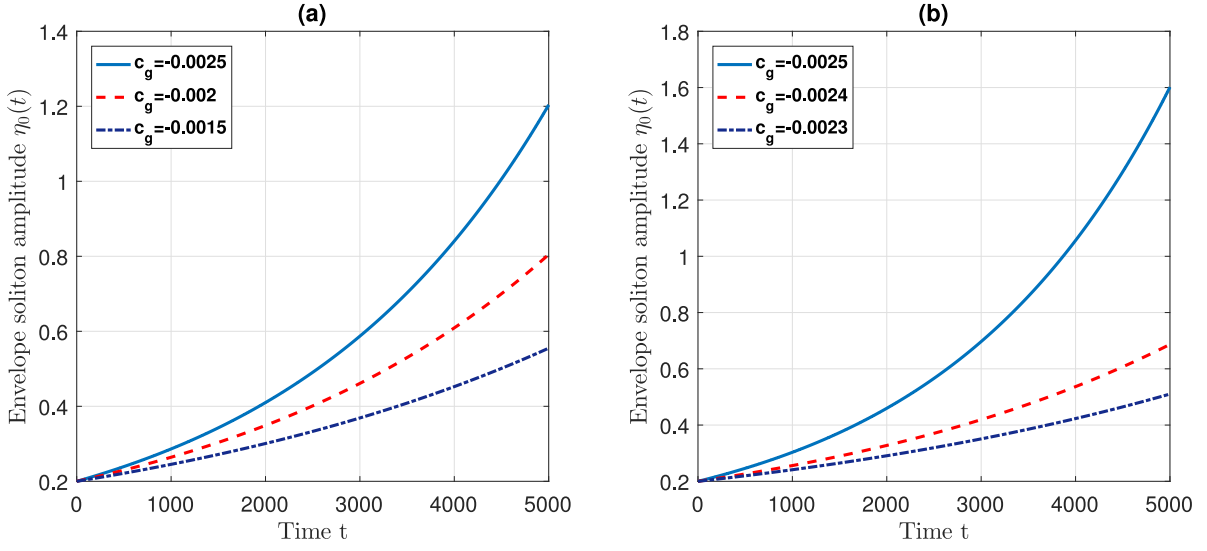

Fig. 3. (Color online) Variations of envelope soliton amplitude $\eta_0(t)$ versus time t for different values of c_g, the imaginary part of group velocity v_g. In panel (a), weak LRI ($s = 10$) and spiking regime ($k_1 = 0.6$) is considered by fixing $D = 0.012$, while in panel (b), strong LRI ($s = 1$) and bursting regime ($k_1 = 1.8$) is examined by fixing $D = 0.0012$. In both cases, we see how envelope soliton amplitude increases with the time and decreases with increasing of c_g.

Of course thanks to the MI proceeding, the soliton-like localized waves known to better ensure storage, transport and transmission of information have proven to be more reliable in many physical systems such as, nonlinear electrical transmission lines [33,34], α-helix proteins [8,9,15,16] and neural networks [10,12,13,19,35] just to cite a few. Usually, the linear stability analysis is performed in order to seek the values range of space parameters which initiate the onset of MI without any information on its longtime evolution. The present analytical contribution aims to improve the method by running the temporal evolution of MI trough the features of the envelope soliton amplitude. Thus, it is shown that any perturbation occurring in the network dynamics exponentially grows in time. This exponential growth rate predicts the appearance of soliton-like localized waves within the network. In order to confirm the existence of the latter, we need to check if the generic model may support these kind of solutions and seek their actions on waves propagation along with chaotic, synchronous and chimera states.

4. Numerical experiments

The discrete instability studied in the previous section allowed us to find the values spectrum of control parameters under which modulated waves could be substantially propagated along the network, but does not give us any information on chaotic behavior, full synchronization or chimera states. The present part aims to unveil these rich properties of the considered neuronal oscillator by numerically solve the generic Eq. (1) while using the above analytical results to formulate initial conditions. To this end, the fourth-order Runge-Kutta computational scheme, periodic boundary conditions and time step $h = 0.01$ are adopted. A network made of $N = 300$ neurons nonlinearly coupled via LR interactions is used, while the range of interaction has been limited to the first twenty neighbors, i.e., $J = 10$. Initial conditions are derived from Eq. (2), while the values 0.01π and $\frac{\pi}{2j}$ were assigned to Q and ν, respectively. In the following, we propose to investigate the onset and the manifestation of chaotic behavior along with synchronization and chimera states within the network under the activation of MI. For this purpose, four specific dynamical regimes, namely: **(I)** weak long-range spiking (WLRS) for $s = 10$ and $k_1 = 0.6$, **(II)** strong long-range spiking (SLRS) for $s = 1$ and $k_1 = 0.6$, **(III)** weak long-range bursting (WLRB) for $s = 10$ and $k_1 = 1.8$ and **(IV)** strong long-range bursting (SLRB) for $s = 1$ and $k_1 = 1.8$, regimes will be widely explored.

4.1. MI and chaotic behavior of neural network

A defining feature of chaos is sensitive dependence on initial conditions. This means that when a given dynamical system exhibits chaotic behavior, a small changes in the state of a system will grow at an exponential rate and will dominate the behavior. Usually chaos is quantified with Lyapunov exponents. These numbers are the long time average exponential rates of divergence of nearby states. If a system has at least one positive Lyapunov exponent, then the system is chaotic. The larger the positive exponent, the more chaotic the system; that is, the shorter the time scale of system predictability. A system may possess any number of Lyapunov exponents, but to confirm chaos we only need to show that the largest Lyapunov exponent (LLE) is positive [36–44].

In order to compute the LLE, we consider the non-perturbed state vector $s_n(t) = \{x_n(t), y_n(t), z_n(t), \phi_n(t)\}$ and the perturbed one $s_{n\iota}(t) = \{x_{n\iota}(t), y_{n\iota}(t), z_{n\iota}(t), \phi_{n\iota}(t)\}$ as a nearby solutions of Eq. (1) with initial conditions $s_n(0)$ and $s_{n\iota}(0)$ such that $|s_n(0) - s_{n\iota}(0)| = \iota << 1$. Thenceforward, the distance between the corresponding trajectories

$$d_n(t) = \sqrt{(x_n(t) - x_{n\iota}(t))^2 + (y_n(t) - y_{n\iota}(t))^2 + (z_n(t) - z_{n\iota}(t))^2 + (\phi_n(t) - \phi_{n\iota}(t))^2}, \tag{14}$$

is used to evaluate the LLE as [37]

$$\lambda_{max} = \lim_{t\to\infty}\lim_{\iota\to 0}\frac{1}{t}\ln\left(\frac{\bar{d}(t)}{\iota}\right), \tag{15}$$

where $\bar{d}(t)$ designates the space average of the distance $d_n(t)$, $\iota = 0.0001$ was selected with an aim of having very close trajectories at the initial time $t = 0$, that is to say $s_{n\iota}(0) = s_n(0) + \iota$. In what follows, each of the four dynamical regimes will be explored and we could follow the impact of MI on chaotic behavior of the network.

In Fig. 4 the LLE, λ_{max}, of each regime is plotted versus the local coupling strength, D. For both WLRS and SLRS regimes, the LLE remains positive thus suggesting that both regimes are unconditionally chaotic regardless the values of control parameters. But, it is worth noticing that SLRS regime is more chaotic than WLRS regime, since its maximum LLE is greater than that of the other. On the other hand, WLRB regime yields a transient chaotic behaviors [22] at $D = 0.01$, i.e., its LLE takes negative value for $D < 0.01$ and remains positive elsewhere for chaotic activities to take place. However SLRB regime is periodic only in the uncoupled ($D = 0$) situation, afterward, it keeps its chaotic character for all non-null D-values. By comparing the maximum values of the LLE in both cases, i.e., WLRB and SLRB regimes, we found that SLRB regime is more chaotic than WLRB one. The data of Table 1 give a general idea on chaotic behavior of the four explored dynamical regimes. This table suggests that the more powerful the localized excitations, the more the system chaotic. In order to be convinced with evidence of chaos, we have plotted the phase portraits of the memristive current $i_n(t) = k_1\left[\cos\left(\phi_n(t)\right)\right]x_n(t)$ versus the membrane potential $x_n(t)$ for a given node n, the results are depicted on Fig. 5.

The panels of Fig. 5 show the chaotic attractors at low level (see panels $(aj)_{j=1,2,3,4}$), then at high level (see panels $(bj)_{j=1,2,3,4}$) of chaos. The panels have been featured for any (s, k_1, D)-values of Table 1. In each panel, the nonlinear 8-shaped Lissajous curves are observed with chaotic features. These Lissajous curves represent a strange chaotic attractors where the basin of the two-scroll attractors is narrowed when MI grows. It is well-established that chaotic neural oscillators make a significant contribution to relevant network behavior [45,46]. Indeed, by means of chaos, neural systems get the ability to adapt, make transitions from one pattern of behavior to another when the environment is altered, and consequently to create a rich variety of patterns [45]. On the other hand Xu et al. [46] showed that chaotic nodes can promote what is known as multi-stable behavior, where the network dynamically switches between a number of different semi-synchronized, meta-stable states. The present contribution which addresses the role of MI along with implications of long-range memory effects on emergency of chaotic states within neural systems agrees with this former results and allows to control chaotic activity in the brain by adjusting either the local coupling strength D, the magnetic coupling strength k_1 or the long-range parameter s.

In order to read the value of the LLE at any value of D and k_1, the network chaotic map is graphed in Fig. 6, while considering weak LRI in panel (a) and strong LRI in panel (b). It is observed that when the simulation time t regresses and

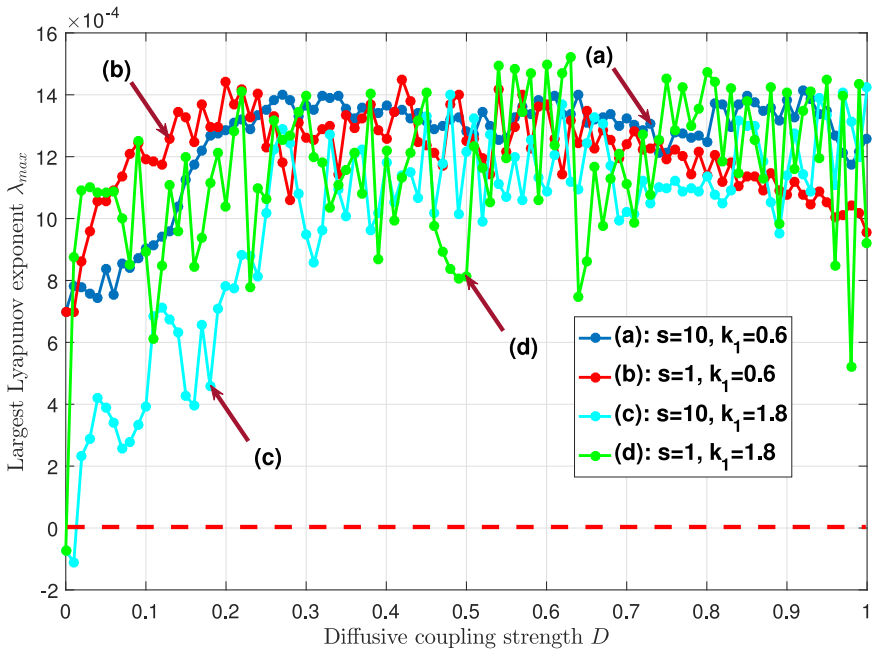

Fig. 4. (Color online) The largest Lyapunov exponent λ_{max} as a function of diffusive coupling strength D for weak ($s = 10$) and strong ($s = 1$) LRIs in spiking ($k_1 = 0.6$) and bursting ($k_1 = 1.8$) regimes. Positive and negative values of λ_{max} correspond to a chaotic and quasi-periodic regimes, respectively.

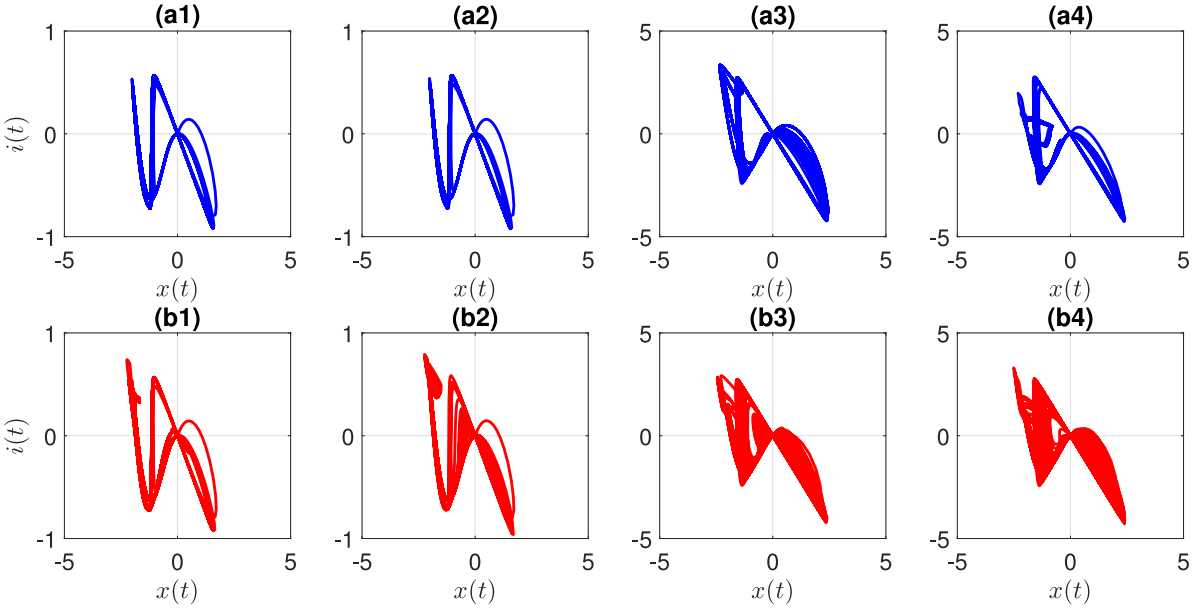

Fig. 5. (Color online) Chaotic attractors at low level of chaos in panels $(aj)_{j=1,2,3,4}$ and at high level of chaos in panels $(bj)_{j=1,2,3,4}$ as shown in Table 1. Panels (a1) and (b1) characterize regime-**(I)**, (a2) and (b2) are for regime-**(II)**, (a3) and (b3) for regime-**(III)**, while (a4) and (b4) correspond to regime-**(IV)**.

the number N of interacting neurons decreases, the neural network is found in a steady chaotic state since the LLE takes only positive values. On each map, the concentrated yellowish areas represent the regions of high chaos whereas the bluish areas are those where the phenomenon of chaos is moderate. Shortly, strong long-range memory effects may induce and emphasize the chaotic dynamical behavior of neural networks.

4.2. MI and neural network synchronicity

There exists different ways to investigate the stability of neural synchronization [44,47]. Here we have adopted the synchronization factor [2,21] to evaluate the degree of network synchronicity during propagation of LR modulated waves within

Table 1
Minimum and maximum values of the positive LLE λ^{+}_{max} at specific values of the diffusive coupling strength D for spiking and bursting regime in weak and strong LRIs. The table allows to quantify low (for each λ_{min}) and high (for each λ_{max}) levels of chaos within the network under the change of the control parameters.

	s=10				s=1.0			
k_1	0.6		1.8		0.6		1.8	
D	0.04	0.92	0.02	1	0.01	0.42	0.98	0.63
$\lambda(\times 10^{-4})$	λ_{min}=7.43	λ_{max}=14	λ_{min}=2.34	λ_{max}=14	λ_{min}=7	λ_{max}=15	λ_{min}=5.2	λ_{max}=15

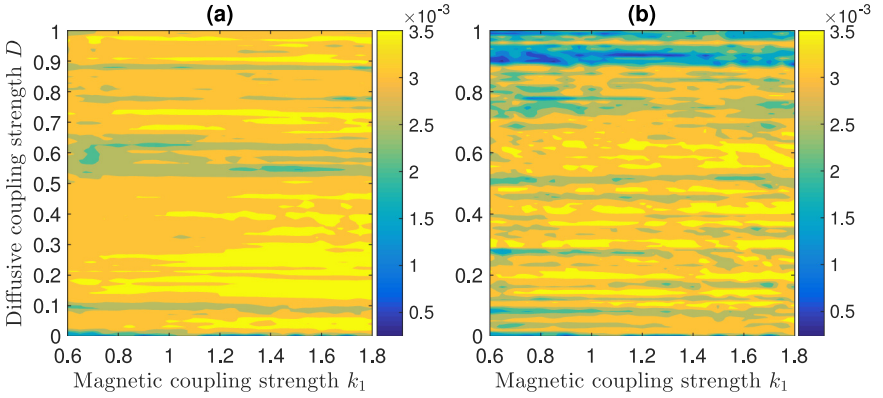

Fig. 6. (Color online) Distribution for the largest Lyapunov exponent λ_{max} in $k_1 - D$ plane in weak LRI (on panel (a)) and strong LRI (on panel (b)) in a small network lattice ($N = 100$) during a short time period $t_{max} = 2000$. Only positive Lypunov exponents are detected thus highlighting the chaotic behavior of the network.

neural network, especially when the phenomenon of electromagnetic induction is considered as a genuine neuro-stimulator. Indeed, the synchronization factor is defined as

$$R = \frac{\left\langle \bar{x}^2(t) \right\rangle - \left\langle \bar{x}(t) \right\rangle^2}{\frac{1}{N}\sum_{n=1}^{N}\left[\left\langle x_n^2(t)\right\rangle - \left\langle x_n(t)\right\rangle^2\right]}, \quad \bar{x}(t) = \frac{1}{N}\sum_{n=1}^{N} x_n(t), \tag{16}$$

where $< \cdot >$ denotes the time averaging. The quantity $\bar{x}(t)$ designates space average of membrane potential. The parameter R allows to measure the synchronization degree of a given network. The values of R are between 0 and 1, and it increases with decreasing average membrane potential errors. It is believed that when the values of R are near to unit ($R \sim 1$), the network reaches its synchronicity state. However, the small values of R (when R converges towards zero) give rise to an unsynchronized states. In what follows, we will firstly examine the synchronicity states of the network via the spatial distribution of synchronization factor R, then select a suitable values of space parameters to present some MI features of membrane potential which should necessary be affected by LR parameters.

The features of Fig. 7 show the variation of the synchronization factor R versus the local coupling strength D for all four dynamical regimes as in Fig. 4. The curves of Fig. 7 give us a possibility to find the appropriate value of the coupling strength D for which the level of synchrony is either high or low. A simple analysis of these curves shows that the slightly unstable regimes, i.e., spiking regime and bursting one in weak LRI would reach their perfect synchronization states at weak local coupling, since the high values of synchronization factor are detected for the low values of synaptic coupling strength D as presented on Table 2. These results predict that at weak local coupling, either in weak or strong LRIs, spiking regime is more synchronously stable than bursting regime which is more modulationally unstable than the former. By comparing these results with those found on chaos investigation, we can conclude that at weak local coupling, the more the regime is modulationally unstable, the more it is chaotic and the less it is synchronous and, reciprocally. Now, concerning the highly unstable regimes, i.e., spiking regime and bursting one in strong LRI, we notice that high values of the synchronization factor are reached at strong local coupling. For example we found that when $D = 0.62$ then $R_{max} = 0.8664$ for SLRS regime and when $D = 0.99$, $R_{max} = 0.7903$ for SLRB regime. These results predict that SLRS regime is more sensitive in accomplishing of synchronization than SLRB regime which in turn is more modulationally unstable and more chaotic than the former. As the phenomenon of neural synchronization is involved in developing of Parkinson states within the brain, it becomes therefore plausible to state and understand that the long-range memory effects may induce Parkinson states in some brain regions

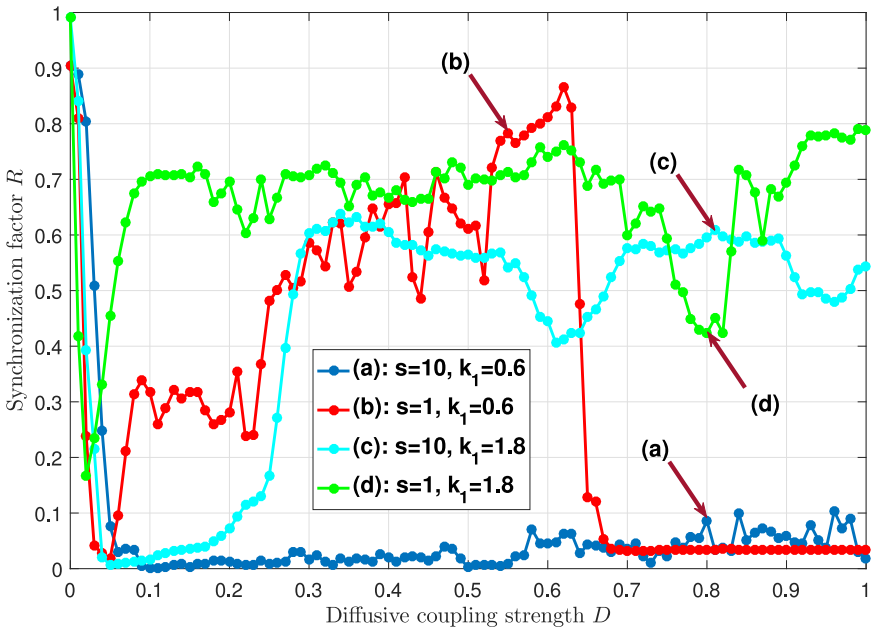

Fig. 7. (Color online) Distribution for synchronization factor R within the magnetized neural network in both weak LRI ($s = 10$) and strong LRI ($s = 1$) under spiking ($k_1 = 0.6$) and bursting ($k_1 = 1.8$) regimes. Panel displays variations of synchronization factor R as a function of diffusive coupling strength D. Large values of R predict a high synchronization level, while small values of the same parameter predict low synchronization level within the network.

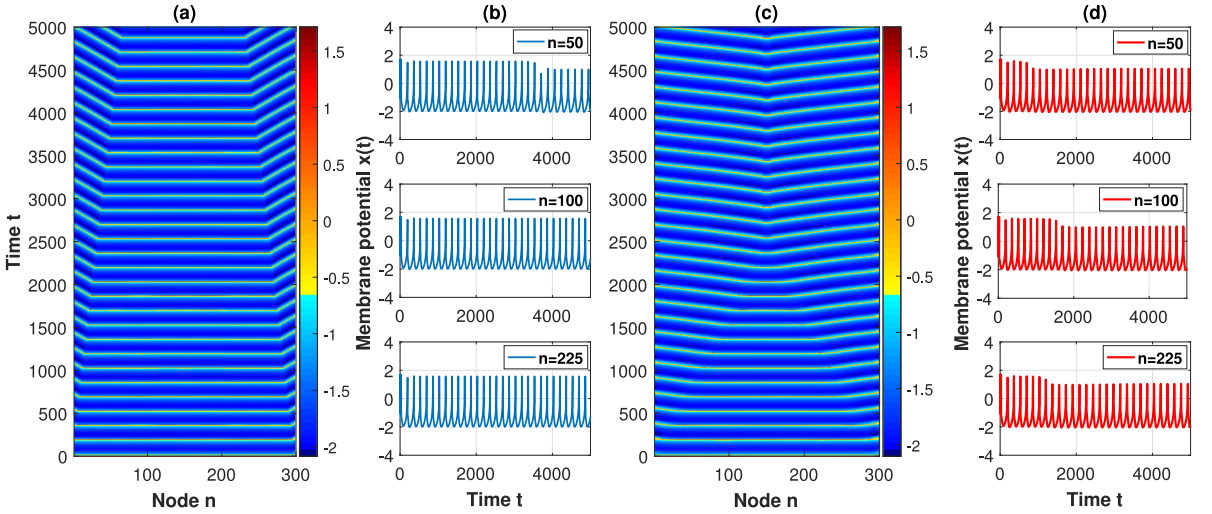

Fig. 8. (Color online) Features of membrane potential $x_n(t)$ at low level of synchronization ($R \to R_{min}$), for spiking regime ($k_1 = 0.6$). Panels (a) and (c) describe the spatiotemporal dynamics of membrane potential. Panels (b) and (d) are time series of three different nodes, $n = 50$, $n = 100$ and $n = 225$. Panels (a) and (b) correspond to weak LRI ($s = 10$), while panels (c) and (d) correspond to strong LRI ($s = 1.0$). We have selected $D = 0.1$ for $R = 0.0010$ in (a)-(b), and $D = 0.05$ for $R = 0.0184$ in (c)-(d). The appearance of spiking-like chimera states within the network is observed.

during short-term memory effects. However, during long-term memory effects, these Parkinson states may simply either be annihilated or blocked.

Furthermore, the specific values of Table 2 are used to highlight the main features of membrane potential. Firstly we consider the low level of synchronization (when $R \to R_{min}$) for WLRS and SLRS regimes. The results are presented in Fig. 8 where the spatiotemporal dynamics of membrane potential is displayed in panels (a) and (c), whereas time series of three different nodes $n = 50$, $n = 100$ and $n = 225$ are depicted in panels (b) and (d). Panels (a)-(b) correspond to WLRS regime, while panels (c)-(d) correspond to SLRS regime. In reminder, according to the investigation on chaotic activity, spiking regimes exhibit only chaotic behavior regardless to the control parameters values. Therefore, in both regimes it is observed that the spatiotemporal dynamics of membrane potential displays a chaotic chimera states while a chaotic spiking patterns are observed in time series features. A similar behavior is observed in Fig. 9 where same features are presented but in bursting

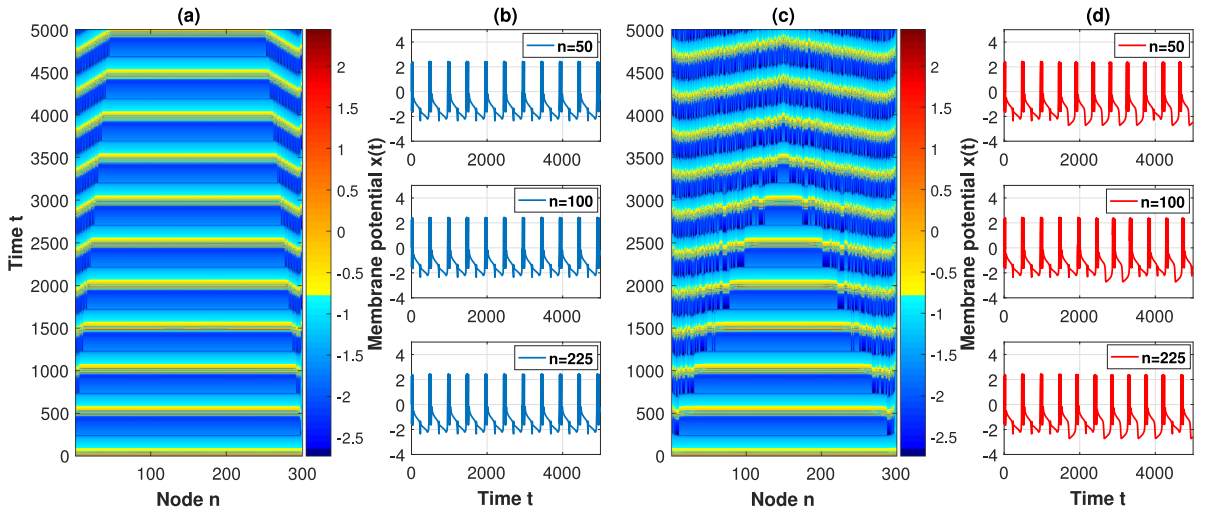

Fig. 9. (Color online) Features of membrane potential $x_n(t)$ at low level of synchronization ($R \to R_{min}$), for bursting regime ($k_1 = 1.8$). Panels (a) and (c) describe the spatiotemporal dynamics of membrane potential. Panels (b) and (d) are time series of three different nodes, $n = 50$, $n = 100$ and $n = 225$. Panels (a) and (b) correspond to weak LRI ($s = 10$), while panels (c) and (d) correspond to strong LRI ($s = 1.0$). We have selected $D = 0.05$ for $R = 0.0063$ in (a)-(b), and $D = 0.02$ for $R = 0.1663$ in (c)-(d). The appearance of bursting-like chimera states within the network is observed.

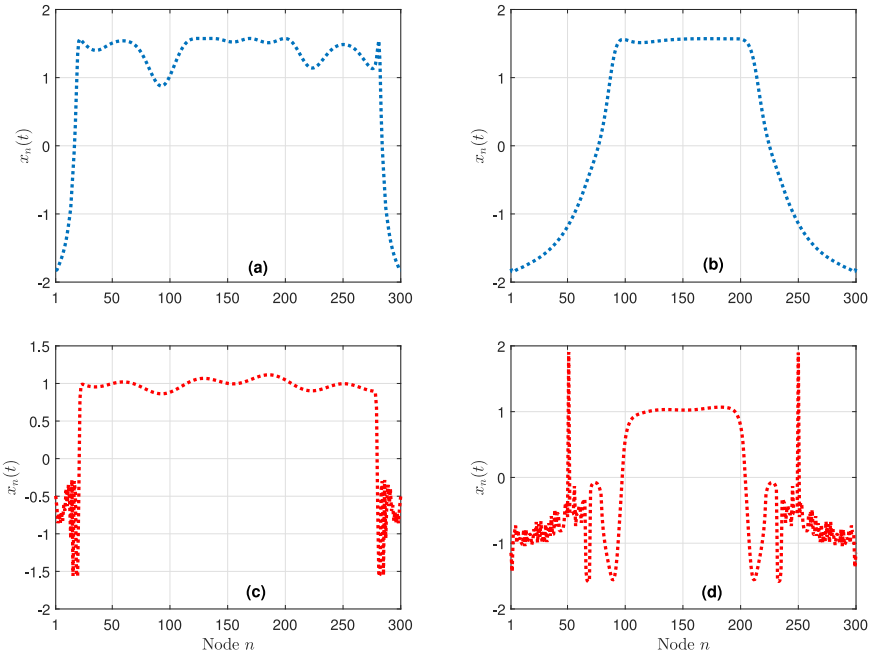

Fig. 10. (Color online) The snapshots of the membrane potential $x_n(t)$ of all neurons in neural network at low level of synchronization ($R \to R_{min}$). A specific time t was selected as $t = 1197$ in (a)-(b) and $t = 1974$ in (c)-(d). Spiking regime ($k_1 = 0.6$) is displayed in panels (a)-(b), while bursting regime ($k_1 = 1.8$) is displayed in panels (c)-(d). Panels (a) and (c) correspond to the weak LRI ($s = 10$), while panels (b) and (d) are for strong LRI ($s = 1.0$). Diffusive coupling strength D was selected as $D = 0.1$ for $R = 0.0010$ in (a), $D = 0.05$ for $R = 0.0184$ in (b), $D = 0.05$ for $R = 0.0063$ in (c) and $D = 0.02$ for $R = 0.1663$ in (d), R being the synchronization factor.

regimes. Indeed, a chaotic chimera states are clearly observed in panels (a) and (c), while chaotic bursting patterns are observed in panels (b) and (d). Remarkably, in WLRS and WLRB regimes, coherent states dominate over incoherent one, that is to say in both regimes, a great number of neurons oscillate synchronously, while only a few cells fire asynchronously. However, an opposite behavior is observed for SLRS and SLRB regimes. Indeed, one can observe how asynchronous states widely dominate over synchronous one. For example we can estimate 33 percent of neurons assembly which synchronize for a short period and then remain in an asynchronous state.

To emphasize on the prediction of chimera-like states in the explored model, the snapshots of membrane potential $x_n(t)$ of all neurons in the network at a given time t are presented in Fig. 10 for all four dynamical regimes. We can see in the

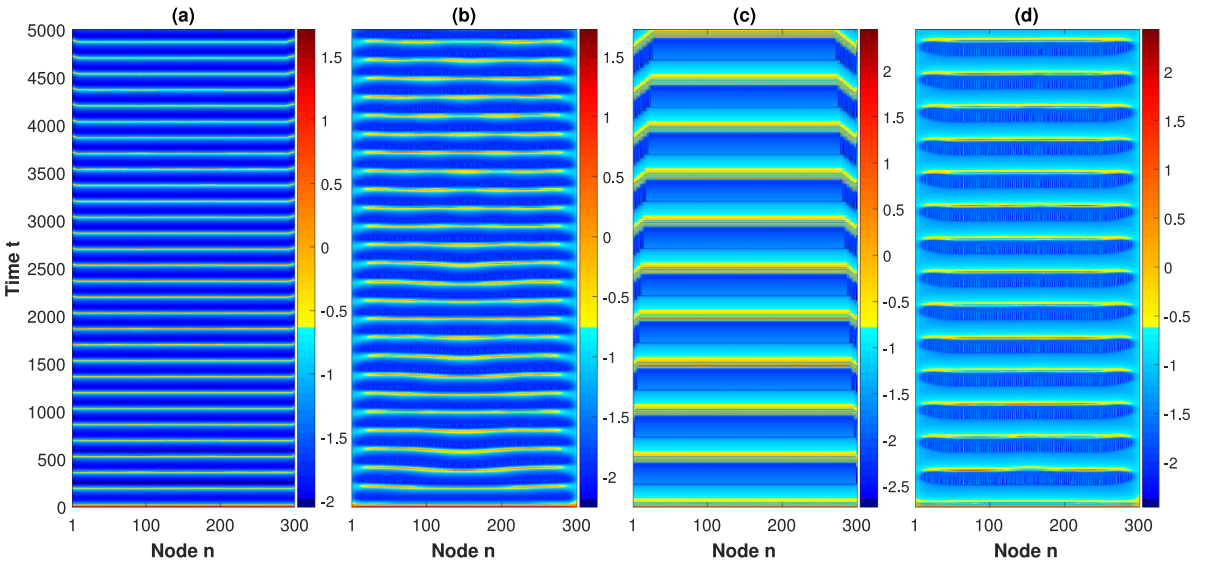

Fig. 11. (Color online) Spatiotemporal dynamics of membrane potential $x_n(t)$ at high level of synchronization ($R \to R_{max}$), for spiking regime ($k_1 = 0.6$) in (a)-(b) and bursting regime ($k_1 = 1.8$) in (c)-(d). Panels (a) and (c) correspond to the weak LRI ($s = 10.0$), while panels (b) and (d) are for strong LRI ($s = 1.0$). The corresponding coupling intensity D is such that $D = 0.01$ for $R = 0.8895$ in (a), $D = 0.62$ for $R = 0.8664$ in (b), $D = 0.01$ for $R = 0.8404$ in (c) and $D = 0.99$ for $R = 0.7903$ in (d), R being the synchronization factor. Chaotic synchronization is displayed for WLRS regime in (a), SLRS regime in (b), SLRB regime in (d), while non-chaotic synchronization is achieved for WLRB regime in (c).

Table 2
Minimum and maximum values of synchronization factor R at specific values of the diffusive coupling strength D for spiking and bursting regime in weak and strong LRIs. The table allows to quantify low (for each R_{min}) and high (for each R_{max}) levels of network synchronicity under the change of the control parameters.

	s=10				s=1.0			
k_1	0.6		1.8		0.6		1.8	
D	0.1	0.01	0.05	0.01	0.05	0.62	0.02	0.99
R	R_{min}=0.0010	R_{max}=0.8895	R_{min}=0.0063	R_{max}=0.8404	R_{min}=0.0184	R_{max}=0.8664	R_{min}=0.1663	R_{max}=0.7903

corresponding panels that at a given time t, the membrane potential of a subgroup of neurons reaches and keeps a constant value. Consequently, this set of neurons having the same value of the membrane potential produces synchronous dynamical states. In contrast, the regions where the membrane potential changes with the network index n constitute asynchronous states. Hence, we can argue that all four dynamical regimes could exhibit chimera states at specific values of control parameters. The present results are similar to those found by Xu et al. [48] when they investigated chimera states and synchronization behavior in multilayer memristive neural networks. Indeed, chimera states are an hybrid states combining asynchronous and synchronous behaviors in a network of identical coupled oscillators [48–51]. These attractive spatiotemporal patterns are believed to be involved in some physical phenomena such as unihemispheric sleep of dolphins and certain migratory birds [52,53], ventricular fibrillation [54], various types of brain diseases [55,56].

Now at high level of synchronization ($R \to R_{max}$), the spatiotemporal dynamics of membrane potential $x_n(t)$ of all four dynamical regimes are presented in Fig. 11. The results illustrate the formation of synchronous chaotic patterns in panels (a), (b) and (d), while non-chaotic synchronous patterns are observed in panel (c). It should be emphasized that the chaotic behavior of neural dynamics is responsible for the recognition of odors and discrimination [57]. Indeed, it has been demonstrated that neural dynamics are heavily dependent on chaotic activity which allows neural system to add a new odor to its repertoire of learned odors [57]. Furthermore, based on the maximum values of the synchronization factor for all four regimes, we can argue that WLRS and SLRS regimes might be more synchronously stable than WLRB and SLRB regimes.

The simulation results of Fig. 12 are some chaotic attractors at low and high level of synchronization by considering the four dynamical regimes, namely, WLRS in (a1) and (b1), SLRS in (a2) and (b2), WLRB in (a3) and (b3), finally, SLRB in (a4) and (b4). The nonlinear 8-shaped Lissajous curves are still observed with chaotic behavior because, in each case the LLE keeps a positive value. These Lissajous curves form a two-scroll attractors which appear to be very sensitive to the change of either the magnetic coupling strength k_1 or the LR parameter s. It is important to mention that the modulation between

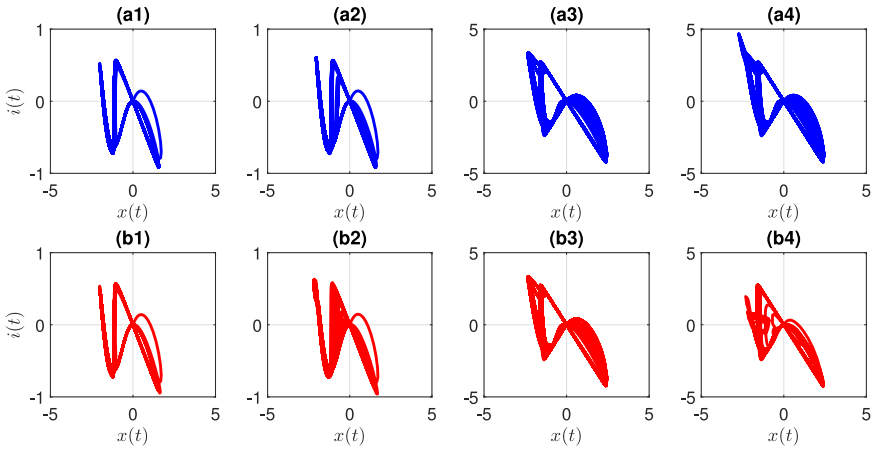

Fig. 12. (Color online) Chaotic attractors at low level of synchronization in $(aj)_{j=1,2,3,4}$, then at high level of synchronization in panels $(bj)_{j=1,2,3,4}$ as shown in Table 2. Panels (a1) and (b1) characterize regime-**(I)**, (a2) and (b2) are for regime-**(II)**, (a3) and (b3) for regime-**(III)**, while (a4) and (b4) correspond to regime-**(IV)**.

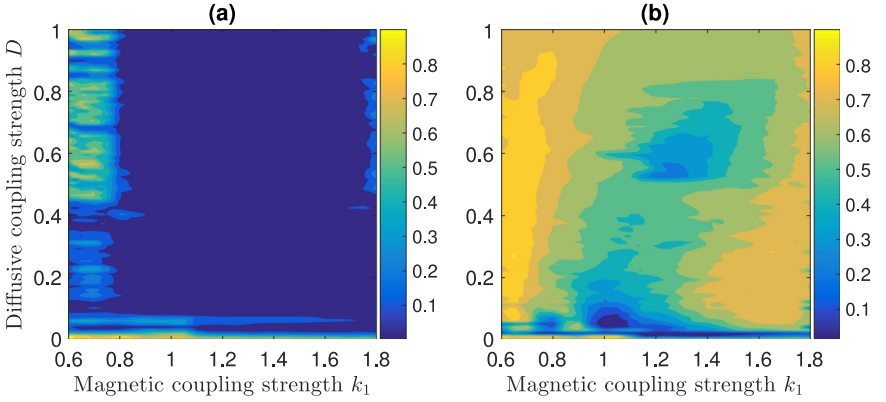

Fig. 13. (Color online) Distribution for the synchronization factor R in $k_1 - D$ plane in weak LRI (on panel (a)) and strong LRI (on panel (b)) in a small network lattice ($N = 100$) during a short time period $t_{max} = 2000$. These features show that more than weak LRI, strong LRI may yields a large spectrum of (k_1, D)-values where chaotic synchronous patterns are expected.

magnetic flux and membrane potential could be generally realized at two different frequencies, one being associated with free oscillations of neural system, and the other, with the fluctuation of magnetic field of intracellular medium. For a such situation of frequency modulation, the chimera states may be understood as an hybrid states where the modulator frequency is sometimes equal, sometimes different from that of resonator. In that sense, the phase portraits presented in Fig. 12 may be useful in controlling of chimera states stability while slowing down or by accelerating the phenomenon of amplitude resonance. Accordingly, when the two frequencies are equal the network may reach a synchronous states.

Lastly, we present in Fig. 13 the synchronization map of a small neural network including only 100 neurons acting for a short time period $t = 2000$. On the left panel (a), weak LRI is considered and gives us possibility to expect synchronous neural network activity only at weak local coupling strength in spiking regime. An increasing in parameters D or k_1 dissipates the synchronization energy and yields blue non-patterned regions in which neural synchronicity is very poor. On the other hand, the right panel (b) displays effects of strong LRI on synchronization activity. As that is observed, strong LRI yields a large spectrum of (k_1, D)-values where synchronous chaotic patterns are expected.

In short, the dependence between the synchronization factor R of the explored neural network, and the synaptic coupling strength D allowed us to observe either quasi-synchronous patterns or chimera states for some specific values of the parameter D. However, if synchronous and asynchronous states can be well characterized by the synchronization factor, chimera (or hybrid) states on the other hand, cannot be highlighted by this parameter. It is therefore important to explore the existence of these hybrid states using certain statistical measures such as strength of incoherence [58].

4.3. MI and characterization of chimera patterns

In recall, a chimera state is the spatial coexistence of coherent (synchronous) and incoherent (asynchronous) dynamics in a network of coupled oscillators, at specific parameter values. There exists several parameters including, strength of in-

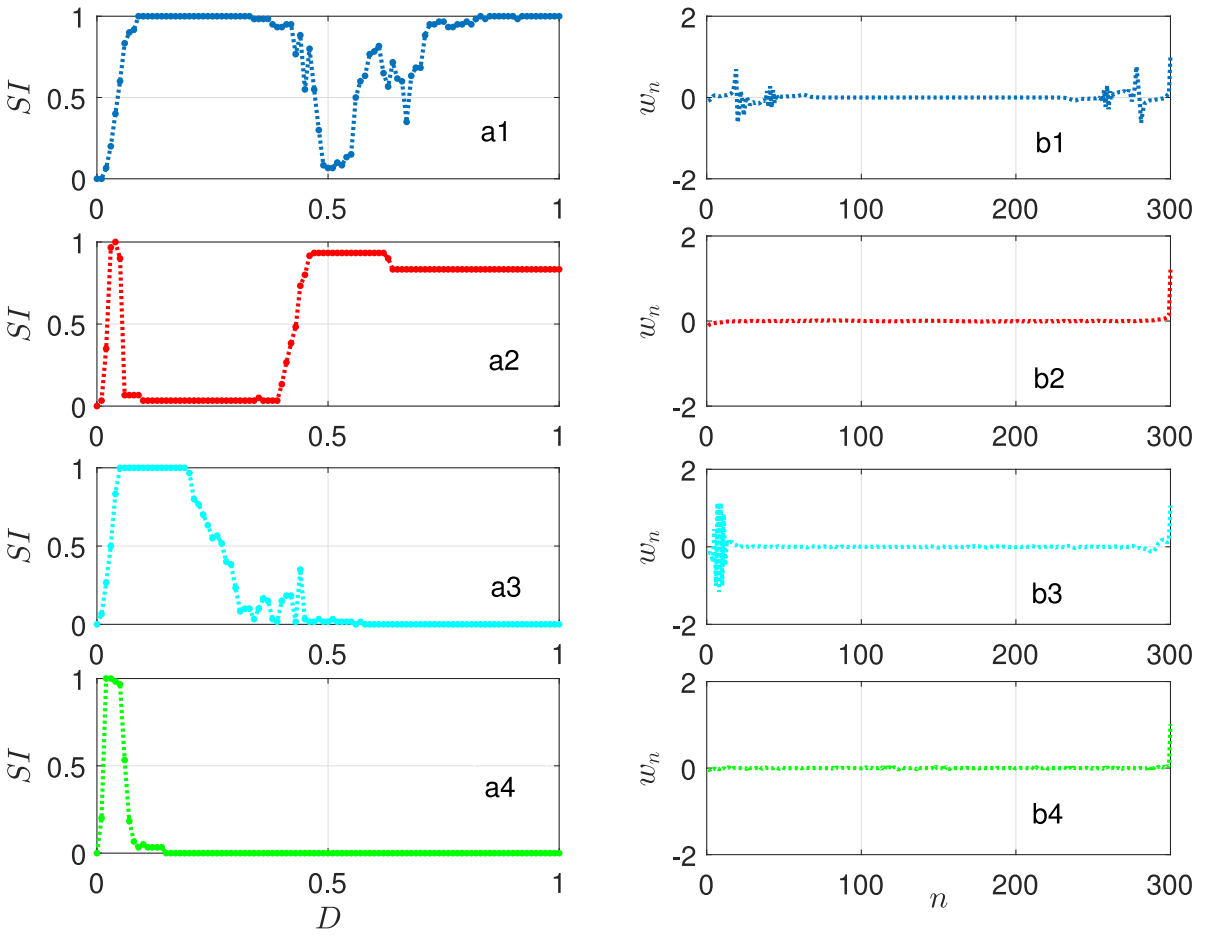

Fig. 14. (Color online) Strength of incoherence *SI* versus diffusive coupling strength *D* in panels $(aj)_{j=1,2,3,4}$. Panels $(bj)_{j=1,2,3,4}$ show the snapshots of the difference variable w_n for each neuron n in neural network at $t = 2000$. From top to bottom, we have WLRS regime in (a1)-(b1), SLRS regime in (a2)-(b2), WLRB regime in (a3)-(b3) and SLRB regime in (a4)-(b4). In panels $(bj)_{j=1,2,3,4}$, we fixed $D = 0.5$ in (b1)-(b3) and $D = 0.1$ in (b4) for chimera state domain.

coherence (SI), discontinuity measure, mean phase velocities, basin stability measure and master stability function [58–61], allowing to characterize chimera states in a network of coupled oscillators. Here we have adopted parameter SI, recently proposed by Gopal et al.[58] to find the specific values of coupling strength D for which chimera patterns take place within the considered dynamical model. In practice, parameter SI is computed by firstly introducing a difference variable defined as $w_n = x_{n+1} - x_n$ for $n = 1, 2, ..., N$ and dividing the number of oscillators into M (even) bins of equal length $p = N/M$. Then the local standard deviation $\sigma(m)$ is defined as

$$\sigma(m) = \left\langle \sqrt{\frac{1}{p} \sum_{k=p(m-1)+1}^{mp} \left(w_k - \bar{w}\right)^2} \right\rangle, \; m = 1, 2, ..., M, \tag{17}$$

where $\bar{w} = \frac{1}{N}\sum_{n=1}^{N} w_n$ designates the space average of variable w_n and $< \cdot >$ denotes the average over time. The quantity $\sigma(m)$ is calculated for every successive p number of oscillators. From $\sigma(m)$, parameter *SI* is evaluated as

$$SI = 1 - \frac{\sum_{m=1}^{M} s_m}{M}, \; s_m = \Theta(\rho - \sigma(m)), \tag{18}$$

where $\Theta(.)$ is the Heaviside step function, and ρ is a predefined threshold that is reasonably small. Here we fixed $M = 60$ and considered ρ as a certain percentage value of difference between $x_{n,max}$ and $x_{n,min}$. Accordingly, $SI = 1$ for incoherent, $SI = 0$ for coherent and $0 < SI < 1$ for chimera states, respectively.

Results of Fig. 14 describe the evolution of *SI* as a function of local coupling strength D on the left and the snapshots of the difference variable w_n on the right at specific values of parameter D while fixing $t = 2000$. We have considered each of four dynamical regimes: (I) WLRS regime in (a1)-(b1), (II) SLRS regime in (a2)-(b2), (III) WLRB regime in (a3)-(b3) and (IV) SLRB regime in (a4)-(b4). It is noticed that WLRS regime supports synchronous state only when $D \leq 0.01$ and remains either in chimera or in asynchronous states elsewhere. The result is quite consistent with that was predicted by the

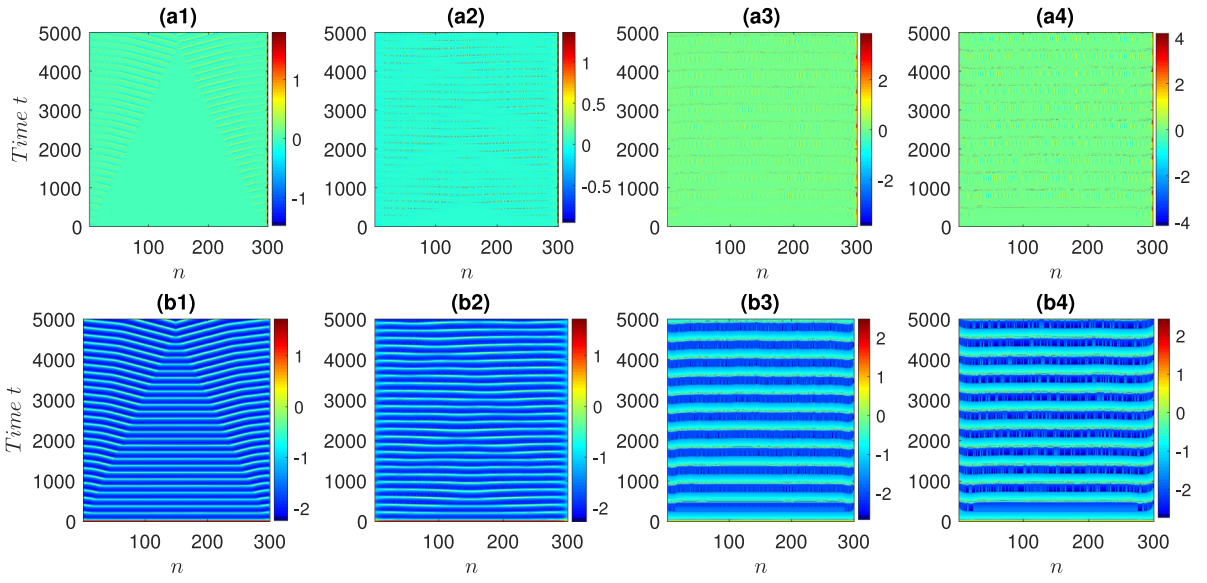

Fig. 15. (Color online) Spatiotemporal plots of difference variable $w_n(t)$ in panels $(aj)_{j=1,2,3,4}$ and membrane potential $x_n(t)$ in panels $(bj)_{j=1,2,3,4}$ for the same scenarios as in Fig. 14. Therein, chimera states are illustrated for each of four dynamical regimes.

synchronization factor R. In reminder, we found that for WLRS regime the maximum value of R is reached for $D = 0.01$, thus leading all neuronal oscillators to a synchronous state. Additionally, the value $D = 0.1$ which is associated to the minimum value of R also coincides with the maximum value $SI = 1$ which translates incoherent behavior of neural network. As regards SLRS regime, it is observed that neural network adopts a chimera state for $D < D_c$, then works incoherently for $D = D_c$ and remains in a chimera state for $D > D_c$, with $D_c = 0.04$. Reasonably, we expected $D_c = 0.05$, value for which the factor of synchronization is minimum instead of $D_c = 0.04$ as observed. This small deviation about the change of rhythmicity of neuronal oscillators can be connected to the chaotic behavior of the network highlighted previously. Furthermore, the value $D = 0.62$ which generates a maximum value of the synchronization factor $R_{max} = 0.8664$ belongs to the chimera state domain, thus suggesting that SLRS regime may be either in a chimera state or in asynchronous state while synchronous state is almost unexpected, except under other specific conditions. About WLRB and SLRB regimes, some similarities are observed. Indeed, for both regimes neuronal activity is characterized by chimera patterns for $0 < SI < 1$, incoherent structures for $SI = 1$ and synchronous state for $SI = 0$, at specific values of parameter D as displayed in panels (a3) and (a4) of Fig. 14. Interestingly, the value of D for which the synchronization factor R is minimal for incoherent states are identical to that for which the strength of incoherence, $SI = 1$, for the same dynamical state. The panels of Fig. 14 $(b_j)_j = 1, 2, 3, 4$ are in perfect agreement with those of Fig. 14 $(a_j)_j = 1, 2, 3, 4$, since the state variable w_n converges toward 0 for coherent states and diverges from 0 for incoherent states, thus suggesting the existence of chimera-like patterns within neural network.

To strengthen the idea on the coexistence of coherent and incoherent modes in the network, the spatiotemporal diagrams of the corresponding chimera states are depicted on Fig. 15. The difference variable $w_n(t)$ and the membrane potential $x_n(t)$ are surfed versus cell number n and time t in panels $(a_j)_j = 1, 2, 3, 4$ and $(b_j)_j = 1, 2, 3, 4$, respectively for the same scenarios as in Fig. 14. Regarding WLRS regime, both (coherent and coherent) states are clearly identifiable. However, for the other regimes coherent state seems to take control over incoherent state, thus confirming that at strong local coupling, the stronger the MI phenomenon, the more synchronous the network [12]. In short, the combined use of the strength of incoherence and the synchronization factor may be helpful to find the accurate values of R, for which a given oscillators network start to synchronize.

5. Conclusion

In this paper, we studied both analytically and numerically modulational instability, chaos, synchronization and chimera states in a diffusively coupled Hindmarsh-Rose neurons. Four dynamical regimes namely weak long-range spiking regime, strong long-range spiking regime, weak long-range bursting regime and strong long-range bursting regime have been explored along with their potential impact on the formation of modulated excitations, chaotic synchronous and chimera states within neuronal network.

Analytically, we found that strong local coupling, high electromagnetic induction and strong long-range interactions importantly support the development of discrete instability within the system. Outstandingly, the critical amplitude and the envelope soliton amplitude as the main MI features are found to be an increasing functions of local coupling strength D and magnetic coupling strength k_1, while the same functions decreased with the increasing of long-range parameter s. Addi-

tionally, the impact of the complex group velocity has been examined. We found that the imaginary part of this parameter largely contributes to the attenuation of the envelope soliton amplitude over the time, although this phenomenon may be inhibited by weaker short-range memory effects.

Numerically, the largest Lyapunov exponents were computed for studying chaos and the synchronization factor was recorded for studying synchronization in neural network. On the one hand, we found that strong long-range memory effects may induce and emphasize the chaotic dynamical behavior of neural networks. On the other hand, the results on synchronization predicted that either in weak or strong LRIs, spiking regime is more synchronously stable than bursting regime which is more modulationally unstable than the former, especially at weak local coupling. By comparing the results on synchronization with those found on chaos investigation, we can conclude that at weak local coupling the more the regime is modulationally unstable, the more it is chaotic and the less it is synchronous and, reciprocally. However, when the local coupling strength became greater, we observed that the powerfully localized modes were also more chaotic and more synchronously stable.

Thanks to statistical measures such as the strength of incoherence, chimera states were elucidated according to the values of the synaptic coupling parameter D. As a result, WLRS regime can adopt the synchronicity state only for low values $(0 < D \leq 0.01)$ of D. For other values of the same parameter, the neural network remains either in a chimera state or in an asynchronous state under WLRS regime. However, under SLRS regime, the neural network operates almost via chimera-like patterns, except for $D = 0.04$ where an asynchronous regime could be observed. Additionally, WLRB and SLRB regimes could exhibit coherent behavior over a wider spectrum of higher values of the parameter D. However, for both regimes, chimera and asynchronous states can also be obtained for another range of values of D as shown in Fig. 14$(a_j)_j = 1, 2, 3, 4$. In our view, the synchronization factor alone does not allow us to better characterize the phenomenon of neuronal synchronization. This parameter should be coupled with the strength of incoherence in order to find its threshold value which indicates the onset of synchronous neuronal activity.

In conclusion, the combination between long-range interactions and electromagnetic induction phenomenon induces long-range memory effects in neural network. The latter produce a rich neural activity including, quasi-periodic synchronous patterns, chaotic and non-chaotic patterns, chimera's, asynchronous and synchronous states, strange chaotic and non-chaotic attractors. All these patterns contribute not only in efficient information processing in the brain in a normal process, but may also be a potentials precursors of some brain injuries such that epileptic seizures, Parkinson and Alzheimer diseases in case of cerebral dysfunctional.

Recent contributions have shown that the neural system can exhibit a high level of synchronization by just increasing the temperature of the system [47]. Therefore, we will attempt to study in the near future, the influence of temperature on chaotic, chimera and synchronous states within neural systems during short or long-range memory effects.

Declaration of competing interest

No author associated with this paper has disclosed any potential or pertinent conflicts which may be perceived to have impending conflict with this work.

CRediT authorship contribution statement

Armand S. Etémé: Conceptualization, Data curation, Methodology, Formal analysis, Investigation, Software, Writing - review & editing. **Conrad B. Tabi:** Data curation, Resources, Software, Writing - original draft. **Alidou Mohamadou:** Supervision, Validation. **Timoléon C. Kofané:** Supervision, Validation.

Acknowledgement

The authors would like to express their deep gratitude to the anonymous referees who have largely contributed to the improvement of the present work. The corresponding author (A.S. Etémé) acknowledges Dr T.L.M. Djomo Mbong for his relevant guidance on the computation of LLE.

Supplementary material

Supplementary material associated with this article can be found, in the online version, at doi:10.1016/j.cnsns.2020.105208.

References

[1] Wu F, Wang C, Xu Y, Ma J. Sci Rep 2016;6:28.
[2] Etémé AS, Tabi CB, Mohamadou A. Commun Nonlinear Sci Numer Simulat 2019;72:432–40.
[3] FitzHugh R. Biophys J 1961;1:445.
[4] Hindmarsh JL, Rose RM. Proc R Soc London Ser-B 1984;221:87.
[5] Spillmann L, Werner JS. Trends Neurosci 1996;19:428–34.
[6] Tabi CB, Mohamadou A, Kofané TC. Eur Phys J E 2010;32:327–32.
[7] Okaly JB, Mvogo A, Woulache RL, Kofané TC. Commun Nonlinear Sci Numer Simulat 2018;55:183–93.

[8] Madiba SE, Tabi CB, Ekobena HPF, Kofané TC. Phys A 2019;514:298–310.
[9] Tabi CB. Chaos Chaos Solitons Fractals 2018;116:386–91.
[10] Tabi CB, Maïna I, Mohamadou A, Ekobena HPF, Kofané TC. Phys A 2015;1:435.
[11] Mvogo A, Tambue A, Ben-Bolie GH, Kofané TC. Commun Nonlinear Sci Numer Simulat 2016;39:396–410.
[12] Etémé AS, Tabi CB, Mohamadou A. Chaos Soliton Fract 2017;104:813.
[13] Etémé AS, Tabi CB, Mohamadou A. Commun Nonlinear Sci Numer Simulat 2017;4(3):211.
[14] Tabi CB, Etémé AS, Mohamadou A. Phys A 2017;474:186.
[15] Tabi CB, Ondoua RY, Fouda HPE, Kofané TC. Phys Lett A 2016;380:2374–81.
[16] Ondoua RY, Tabi CB, Fouda HPE, Mohamadou A, Kofané TC. Eur Phys J B 2012;85:318.
[17] Mvogo A, Ndzana FII, Kofané TC. Wave Motion 2019;84:46–55.
[18] Leon J, Manna M. Phys Rev Lett 1999;83:2324.
[19] Kakmeni FMM, Inack EM, Yamakou EM. Phys Rev E 2014;89:052919.
[20] Tabi CB, Etémé AS, Mohamadou A, Kofané TC. Chaos Solitons Fract 2019;123:116–23.
[21] Etémé AS, Tabi CB, Ateba JFB, Ekobena HPF, Mohamadou A, Kofané TC. J Phys Commun 2018;2:125004.
[22] Bao BC, Liu Z, Xu JP. Electron Lett 2010;46.
[23] Muthuswamy B. Int J Bifurcat Chaos 2010;20:1335.
[24] Ma J, Wu F, Hayat T, Zhou P, Tang J. Phys A 2017;486:508.
[25] Takembo CN, Mvogo A, Ekobena HPF, Kofané TC. Int J Mod Phys B 2018;32:1850165.
[26] Takembo CN, Mvogo A, Ekobena HPF, Kofané TC. Nonlinear Dyn 2018;95:1067.
[27] Takembo CN, Mvogo A, Ekobena HPF, Kofané TC. Nonlinear Dyn 2019;95:1079.
[28] Leon J, Manna M. J Phys A: Math Gen 1999;32:2845.
[29] Maïna I., Tabi C.B., Mohamadou A., Ekobena H.P.F., Kofané T.C.. Chaos. 2015. 25, 43118.
[30] Vladimir G, Marek S. Phys Rev E 2010;81:056602.
[31] Mohamadou A, Fopa F, Kofané TC. Opt Commun 2006;266:648.
[32] Benjamin TB, Feir JE. J Fluid Mech 1967;27:417.
[33] Ndzana FII, Mohamadou A, Kofané TC. J. Phys D: Appl Phys 2007;40:3254–62.
[34] Ndzana F.I.I., Mohamadou A., Kofané T.C.. CHAOS. 2008. 18, 043121.
[35] Nfor NO, Ghomsi PG, Kakmeni FMM. Phys Rev E 2018;97:022214.
[36] Wolf A., Swift J.B., Swinney H.L., Vastano J.A.. Physica. 1985. 16D, 285.
[37] Kantz H. Phys Lett 1994;185:77.
[38] Dabrowski A. Nonlinear Dyn 2012;67:283.
[39] Dabrowski A. Nonlinear Dyn 2014;78:1601.
[40] Balcerzak M, Pikunov D, Dabrowsk A. Nonlinear Dyn 2018;94:3053.
[41] Mbong TLMD, Siewe MS, Tchawoua C. Commun Nonlinear Sci Numer Simulat 2015;22:228.
[42] Tuwa PRN, Miwadinou CH, Monwanou AV, Orou JBC, Woafo P. Mech Res Commun 2019;97:8.
[43] Fotsa RT, Woafo P. Chaos Solitons Fractals 2016;93:48.
[44] Liu Z, Ma J, Zhang G, Zhang Y. Appl Math Comput 2019;360:94.
[45] Rabinovich M.I., Abarbanel H.D.I.. Neuroscience. 1989. 87, 5, 8.
[46] Xu K, Maidana JP, Castro S, Orio P. Sci Rep 2018;8:8370.
[47] Budzinski RC, Baoretto BRR, Prado TL, Lopes SR. Chaos Solitons Fractals 2019;123:35–42.
[48] Xu F, Zhang J, Jin M, Huang S, Fang T. Nonlinear Dyn 2018;94:776.
[49] Majhi S, Perc M, Ghosh D. Sci Rep 2016;6:39033.
[50] Panaggio M.J., Abrams D.M.. Nonlinearity. 2015. 28, R67–R87.
[51] Banerjee T, Dutta PS, Zakharova A, Schöll E. Phys Rev E 2016;94:032206.
[52] Abrams DM, Mirollo R, Strogatz SH, Wiley DA. Phys Rev Lett 2008;101:084103.
[53] Ma R, Wang J, Liu Z. Europhys Lett 2010;91:40006.
[54] Davidenko JM, Pertsov AV, Salomonsz R, Baxter W, Jalife J. Nature(London) 1992;355:349.
[55] Levy R., Hutchison W.D., Lozano A.M., Dostrovsky J.O.. J neurosci. 2000. 20, 7766.
[56] Ayala GF, Dichter M, Gumnit RJ, Matsumoto H, Spencer WA. Brain Res 1973;52:1.
[57] Skarda CA, Freeman WJ. Behav Brain Sci 1987;10:161–95.
[58] Gopal R, Chandrasekar VK, Venkatesan A, Lakshmanan M. Phys Rev E 2014;89:052914.
[59] Rakshit S., Bera B.K., Perc M.z., Ghosh D.. arxiv:1704.05301v1 [nlin.CD] 18 apr. 2017.
[60] Kundu S., Majhi S., Bera B.K., Ghosh D., Lakshmanan M.. arxiv: 1707.08443v1 [nlin.AO] 16 jul. 2017.
[61] Khatun A.A., Jafri H.H.. arxiv:1903.02739v1 [nlin.CD] 7 mar. 2019.